Science Advances
AAAS

advances.sciencemag.org/cgi/content/full/7/3/eabd4449/DC1

Supplementary Materials for

Metallic line defect in wide-bandgap transparent perovskite $BaSnO_3$

Hwanhui Yun, Mehmet Topsakal, Abhinav Prakash, Bharat Jalan, Jong Seok Jeong, Turan Birol, K. Andre Mkhoyan*

*Corresponding author. Email: mkhoyan@umn.edu

Published 15 January 2021, *Sci. Adv.* **7**, eabd4449 (2021)
DOI: 10.1126/sciadv.abd4449

This PDF file includes:

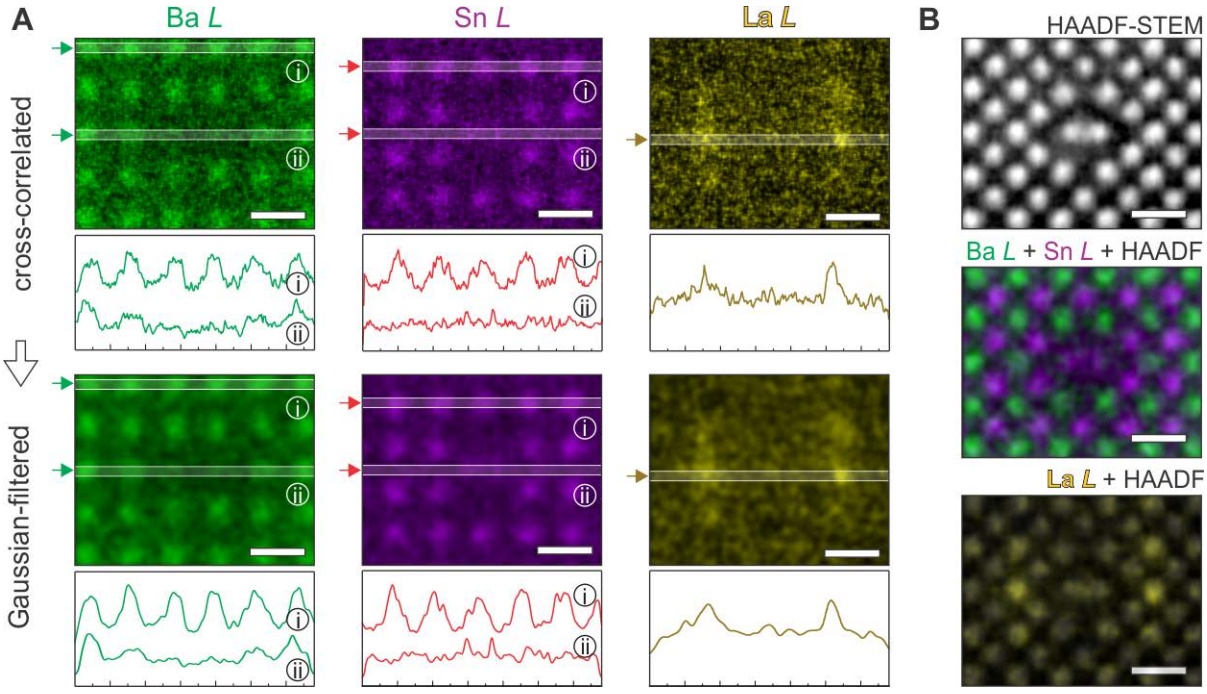

Fig. S1. Image processing of EDX elemental maps. (A) The steps showing how several EDX elemental maps acquired from a line defect were first cross-correlated and then Gaussian-filtered using full-width half maximum (FWHM) of 0.6 Å, which is below the spatial resolution of the STEM. The intensity line profiles extracted from the maps, presented below each map, show reduction of the noise in the maps. The locations of extracted line profiles are indicated by white lines and arrows on the maps. **(B)** Final EDX maps of Sn with Ba and La overlaid with a corresponding HAADF-STEM image. Scale bars are 0.5 nm. These final maps are the maps shown in main text, Fig. 1**(D)**.

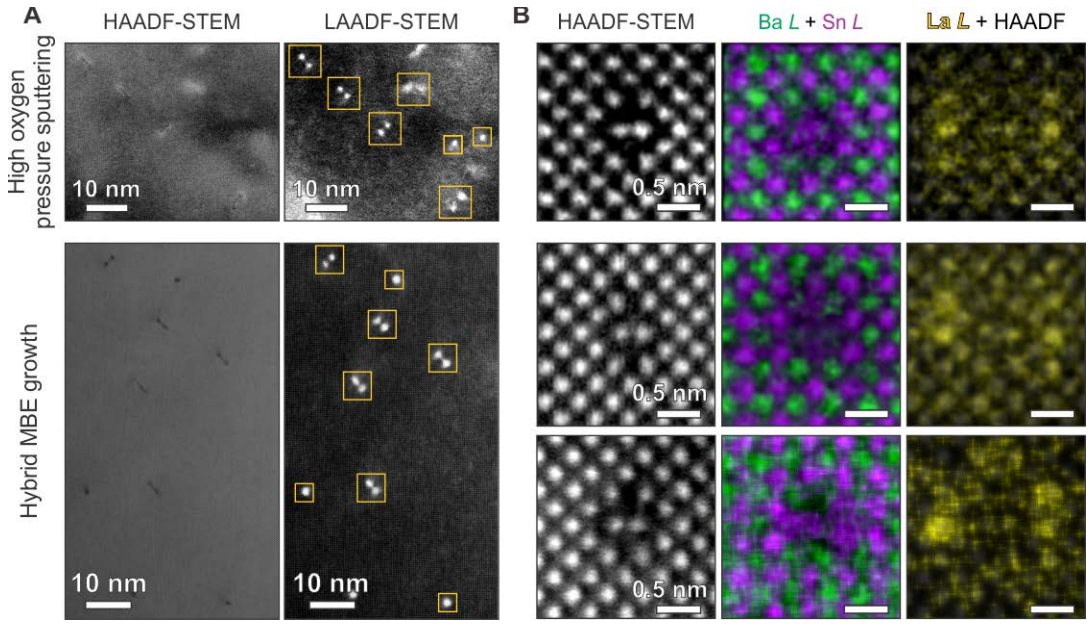

Fig. S2. **ADF-STEM images and EDX elemental maps of the line defect. (A)** Low-magnification plan-view HAADF- and LAADF-STEM images of La:$BaSnO_3$ thin films grown by high oxygen pressure sputtering and hybrid MBE techniques. LAADF-STEM images show presence of many strong spot-like contrast (highlighted in yellow boxes) in all $BaSnO_3$ films. HAADF-STEM images reveal that the contrast originates from either threading dislocations or these line defects. The density of the line defect appears to be dependent on the growth techniques or the strain in the film: about 3×10^2 defect/μm^2 for sputtering-grown La:$BaSnO_3$ films with high strain distribution, and about 30 defect/μm^2 for hybrid MBE-grown La:$BaSnO_3$ films with low strain distribution, based on LAADF image analysis. **(B)** Examples of atomic-resolution HAADF-STEM images and corresponding EDX elemental maps of line defects found in sputtering- and hybrid MBE- grown films, where Sn signal at the core and La signal at nearby atomic sites are visible in all cases.

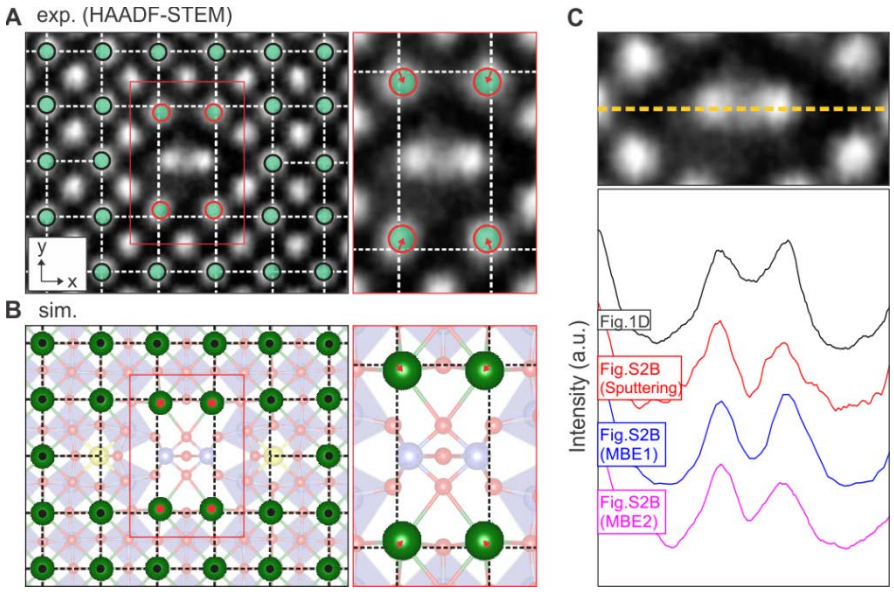

Fig. S3. Displacements of four neighboring Ba columns toward the defect core. (A, B) Experimental HAADF-STEM image and simulated atomic structures of the line defect showing inward displacement of the four neighboring Ba columns. Dash-lines connecting Ba atoms away from the defect core are drawn to visualize the displacement of four neighboring Ba columns relative to their bulk lattice sites. In the magnified images, displacements are indicated by red arrows. Inward displacements of the Ba columns in x- and y-directions were 6% and 15% (experiment) and 5% and 6% (simulation). **(C)** Intensity line profiles from the experimental HAADF-STEM images in Fig. 1**(D)** and SM Fig. S2**(B)** taken across core Sn-Sn pairs of a line defect as shown by a dashed line on the top image. These intensity profiles show variations in intensities in center O atom location as well as in core Sn locations suggesting variations in position and composition of these atomic columns.

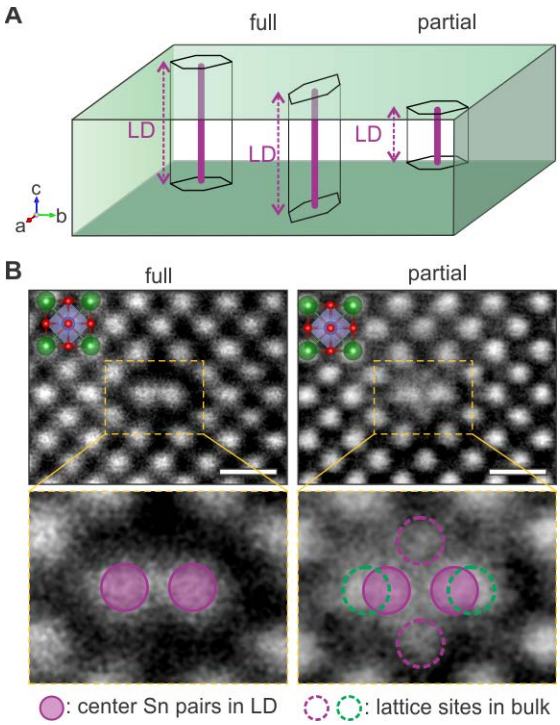

Fig. S4. Full and partial line defects. (A) Illustration of full and partial line defects. **(B)** HAADF-STEM images of full and partial line defects. HAADF-STEM image of the partial line defect shows superimposed contrast of the line defect and bulk $BaSnO_3$. Scale bars are 0.5 nm.

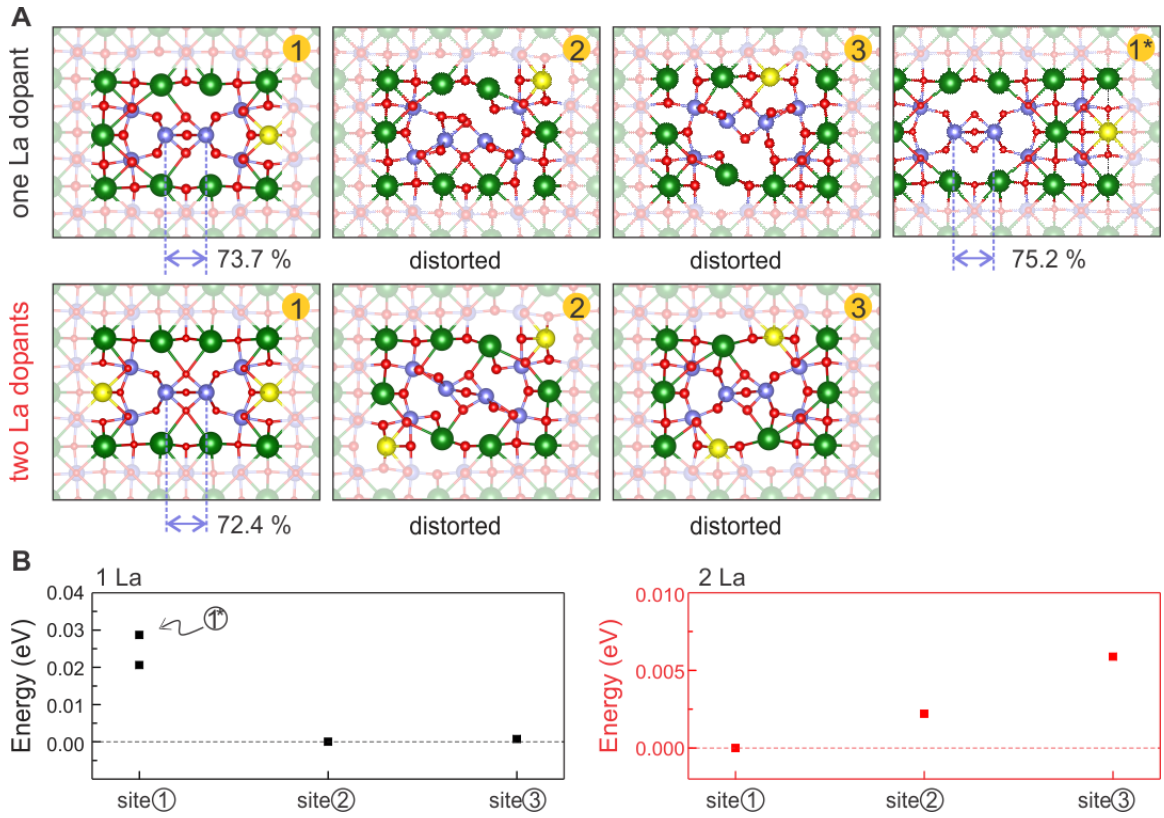

Fig. S5. The structure of the line defect with La dopant at different locations. **(A)** The relaxed atomic structure of the line defect with 1 La dopant (first row) and with 2 La dopants (second row). As La dopants substitute Ba atoms at the position Ba①, the core Sn-Sn distance reduces. **(B)** The relative total energy of each configuration. When comparing one La substitution at Ba① and Ba①* sites, substitution at Ba① site results in lower energy, which indicates the stabilizing effect of La dopants on the line defect when they are close. With only one La dopant, the total energy is lower when La is at sites Ba② or Ba③. However, they lead to asymmetric configurations and dangling oxygen atoms. With 2 La dopants, the defect core is energetically favorable when dopants are at the site Ba①, which is also closer to the experimental observations. When 2 La dopants are located symmetrically at position Ba② or Ba③, as shown in **(A)**, the structure is distorted, but does not introduce dangling oxygen atoms. Based on total energies of the 2 La-doped line defect structures, La will be preferably be located in the order of: Ba①, Ba②, and Ba③ sites, which is consistent with the experimental observations.

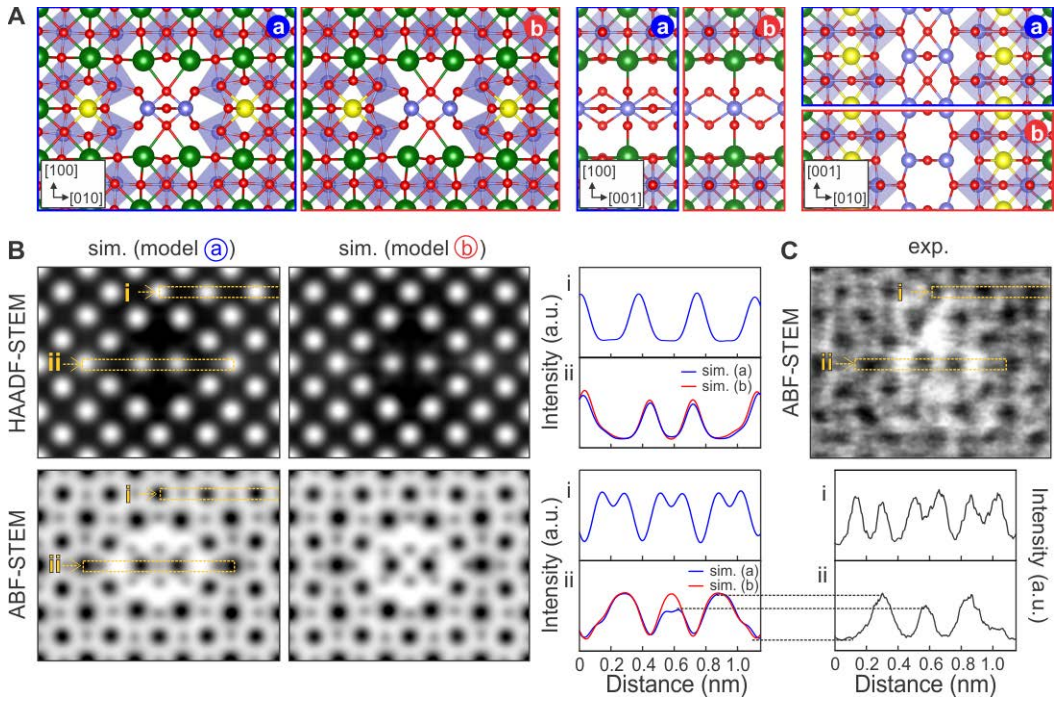

Fig. S6. The structure of line defect with and without oxygen in-between the Sn-Sn pair in the core. **(A)** The atomic structures of line defects after structural relaxation of the models with ⓐ and without ⓑ central oxygen atom, viewed along three major axes. The core Sn-Sn distance of the relaxed structures was $0.724a_0$ and $0.734a_0$ for ⓐ and ⓑ cases, respectively. **(B)** Simulated HAADF- and annular bright-field (ABF)-STEM images of two line defect structures shown in **(A)**. *Multislice* algorithm was used for these simulations. Intensity line profiles were extracted from the bulk $BaSnO_3$ region (i) and the line defect region (ii), as indicated by yellow dotted lines, and plotted on the right panels. While simulated HAADF-STEM images of the two models do not show obvious difference, ABF-STEM images show visible contrast difference at the defect core due to darker contrast generated from the central oxygen. **(C)** Experimental ABF-STEM image of the line defect. The intensity line profile across the line defect core shows lower intensity at the center, which indicates that the structure likely contains oxygen atoms at the center.

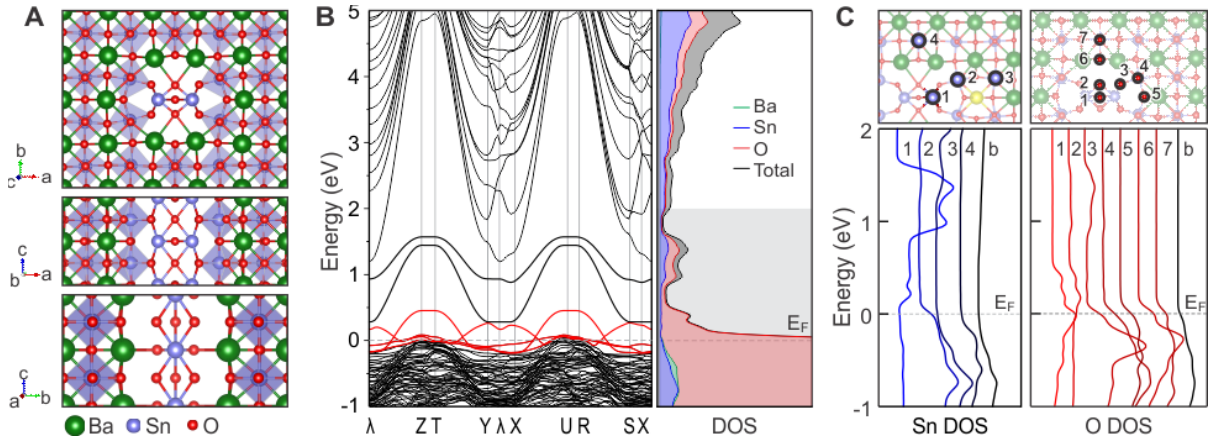

Fig. S7. Computed atomic and electronic structures of the line defect with no dopants. (A) Calculated atomic structure of the line defect viewed along three major axes. The Sn atoms in the defect core are shifted half unit cell along the defect line direction. The calculations also predict minor changes in the atomic structure of the $BaSnO_3$ structure outside defect core (e.g. an octahedral tilt in the surrounding four SnO_6 when viewed in the c-axis). **(B)** Electronic band structures and DOS of the line defect calculated using atomic structure in **(A)**. Metallic bands, the bands that are crossing Fermi energy (E_F = 0) are highlighted in red. Atom-projected DOS indicate that the metallic bands are predominantly from O and Sn atoms. **(C)** Site-projected DOS for Sn and O atoms in the line defect structure. DOS of selected atoms, locations of which are indicated in the schematics on the top, show that the O and Sn atoms of defect core are the ones with metallic characteristics.

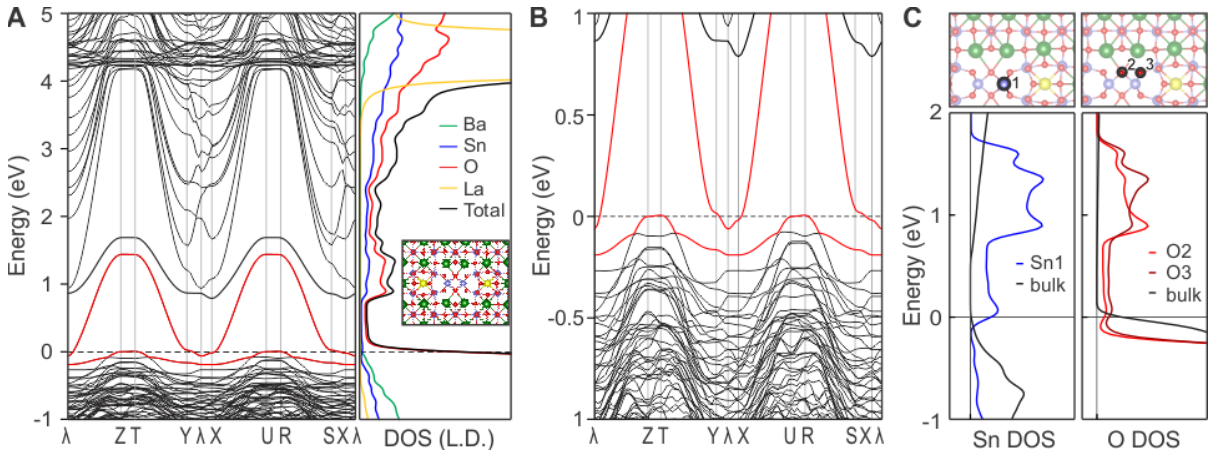

Fig. S8. Computed electronic structures of the line defect with O vacancy at the center. (A) Electronic band structure (left) and DOS (right) of the line defect with missing center oxygen. The atomic model is shown in the inset in the DOS plot. **(B)** Magnified band structure showing E_F-crossing bands. Metallic bands, the bands that are crossing Fermi energy (E_F = 0) are highlighted in red. **(C)** Site-projected DOS for core Sn and O atoms. DOS of selected atoms, locations of which are indicated in the schematics on the top, show that the O and Sn atoms of defect core are the ones with metallic characteristics.

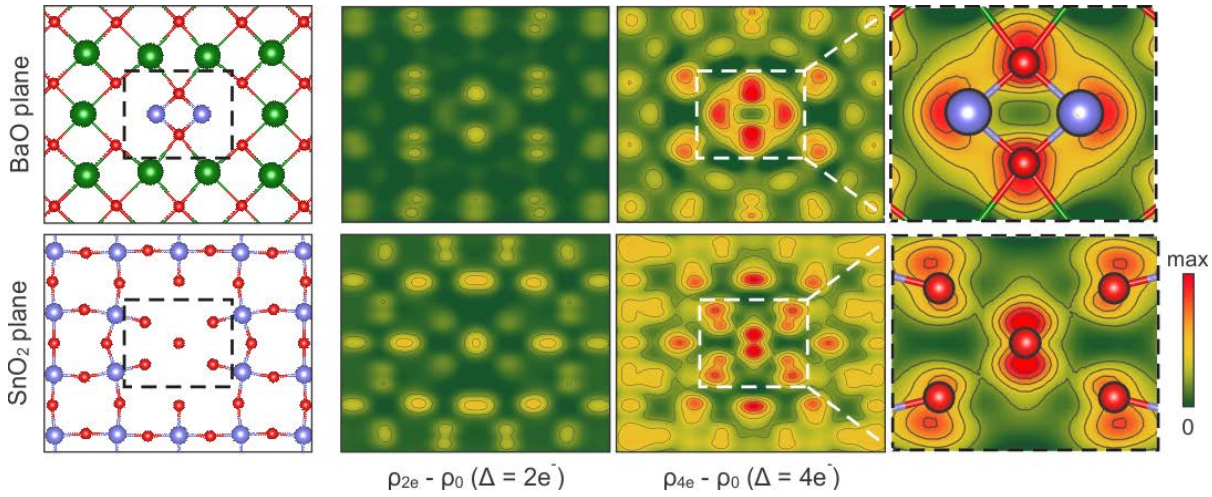

Fig. S9. The effect of additional negative charge on the line defect with no dopants. The atomic arrangements (on the left) and corresponding EDDMs between the additionally charged, with $2e^-$, $4e^-$, and original line defects without La dopants (on the right) for both atomic planes (BaO and SnO_2 planes) perpendicular to defect line direction. Magnified EDDMs of the defect core overlaid with atom model show that most of the additional charge is concentrated at the core O and Sn atoms. Undoped line defect with additional $4e^-$ is similar to 2-La-doped line defect with additional $2e^-$, shown in the main text, Fig. 3**(B)**.

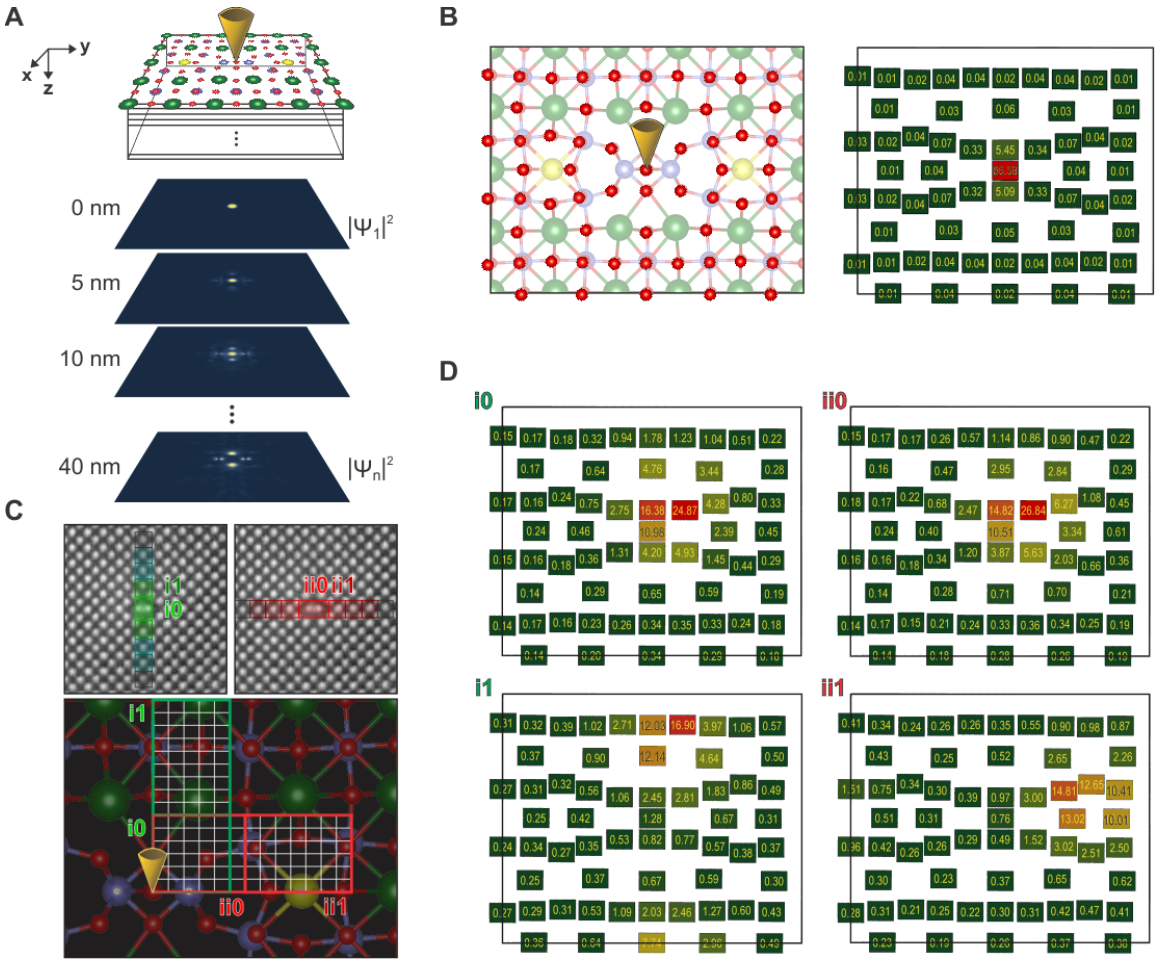

Fig. S10. Evaluation of O *K* edge intermixing in STEM-EELS spectra. Using *Multislice* algorithm, STEM beam propagation in the line defect structure was evaluated and contributions of core-electron excitation from individual oxygen atoms were determined. **(A)** The electron beam intensity distribution at each depth was computed, as shown schematically for a probe located at the center of the line defect. Slice thickness of Δz = 2.055 Å, which is a half of the unit-cell, was used in these simulations and the total thickness of the structure was set to be 40 nm. Beam intensity at each oxygen atom was evaluated by integrating the intensity within the radius of oxygen atom (r_O = 0.73 Å). **(B)** The atomic structure of the line defect with highlighted oxygen atoms used for the integration (left) and the oxygen atom-projected beam intensity map for the probe located at the center (right). On the map, fractions of the beam intensity at each O atomic column (in %) are indicated. In this case of a STEM probe located at the center, final O *K* edge is determined by a weighted average of O *K* edges from the all O atoms on this map with fractions used as weighting coefficients. O *K* edges used for such calculations are shown in Fig. 4**(A)**. For O atoms outside the displayed region, bulk O *K* edge was used. **(C)** To account for the scanning probe in each area used for EELS acquisition, the acquisition areas (i0, i1, ii0, and ii1) were meshed to generate evenly distributed probe positions (with step size of 0.5 Å). The oxygen atom-projected beam intensity maps were calculated for each probe position and averaged for each region. **(D)** The final oxygen atom-projected beam intensity maps for each EELS acquisition areas: i0, i1, ii0, and ii1. Fractions of the beam intensity (in %) are indicated at O atomic columns on each map. By calculating a weighted average of O *K* edges based on the fractions, the O *K* edge spectra for the areas i0, i1, ii0, and ii1 were determined and used in main text, Fig. 4**(C)**.